CHAPTER 4

Structural, Electronic, Lattice Dynamical and Optical Properties of Group-I based Delafossites

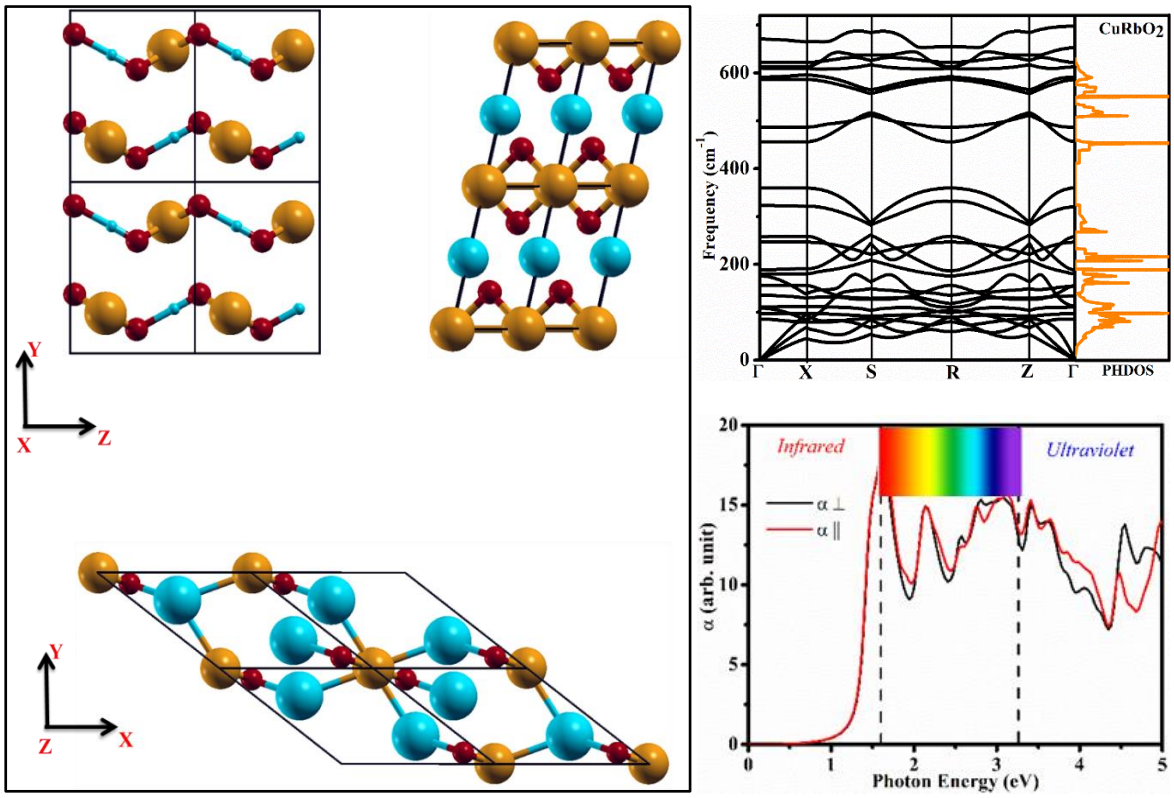

D. Upadhyay, N. Joshi, A. Pratap, and P. K. Jha, *J. Appl. Phys.* **128**, 155701 (2020)

4.1 Introduction

Nowadays, the utility of optoelectronic devices is rising in invisible electronics, functional windows, small circuits, dye-sensitized solar cells (DSSCs) and devices of modern technology [1-3]. The development of exceedingly effective optoelectronic devices is still thought-provoking due to the unavailability of highly conducting p-type semiconductors. Most of the semiconductors such as In_2O_3, ZnO, SnO_2, $CuWO_4$, etc. are of n-type, even though the high efficient optoelectronic devices require both n- and p-type semiconductors for the junction devices [8]. These p-type semiconductors possess low electrical conductivity, which originates mainly due to the localized holes around O atoms owing to strong electronegativity character [9]. The O 2p orbitals are far below to that of metallic atoms and generates deep acceptor levels induced by the holes [10]. The high hole effective mass and low mobility are the barriers of p-type conductivity. The heavy holes require high energy to migrate within the crystal lattice. The localized holes results in less dispersive valence band maximum (VBM) [11,12]. To overcome these drawbacks, Kawazoe et al. [13] introduced a "degree of covalency" in metal-oxygen bonding of traditional delafossite $CuAlO_2$. To modify the valence band edge by mixing orbitals of appropriate counter cations that have energy filled levels comparable to the O 2p levels, which induce the formation of an extended valence band structure in the semiconductors. This practice would diminish the strong Columbic force by O atoms thus delocalizing the holes [12]. However, these efforts are not sufficient yet to achieve the high effectual junction devices and the conductivity of delafossites is still very low compared to n-type materials. The highest p-type conductivity so far observed is 200 Scm^{-1} for Mg doped $CuCrO_2$, but still it is lower than the n-type semiconductors [13]. Far reaching efforts are being made to achieve good p-type conductivity in delafossite oxides. Hautier et al. [14] scanned numerous compounds such as BO_6, $A_2Sn_2O_3$ (A=K, Na), few earth-abundant, and some toxic

candidates such as $PbTiO_3$ and $K_2Pb_2O_3$ to search the best p-type transparent conducting oxides (TCOs) with low effective mass and large band gap. Cerqueira et al. [15] explored Cu, Ag, and Au-based ternary oxides belonging to p-type semiconducting group with a wide range of band gap and low hole effective mass. Shi et al. [16] examined ternary chalcogenide compounds and found $AgYS_2$, KYS_2, and $RbYS_2$ with large band gap and lower effective mass for p-type transparent electrodes.

In conventional delafossites, high p-type conductivity and lower hole mobility are missing due to the lack of Cu–O–Cu linkages [17]. However, high conductivity is observed in $CuCrO_2$ and $CuFeO_2$ due to the favorable mixing of monovalent (M^I) and trivalent cations (M^{III}) [17, 18]. It is noteworthy that the doping of divalent dopants at the trivalent site pointedly enhances the conductivity of delafossite-type oxides [19]. Numerous attempts have been made to increase p-type electrical conductivity by doping of different divalent cations [17-19]. The reasonable decrement in the conductivity is due to the diminution in ionic radius of the M^{III} cations leads to a reduction in the lattice parameters [20]. In Cu^+ oxides, the electronic bands near the Fermi level are accomplished by hole doping, which has the d^{10} closed shell. Hence, VBM is composed of mainly the Cu 3d with some O 2p character. The electrical conductivity of these delafossite oxides depends on the strong p-d hybridization. Suitable mixing of monovalent and trivalent cations may increase the conductivity. Apart from this, several delafossite oxides have been synthesized as new chemical compositions with a variety of crystal symmetries, for pointing towards the low hole effective mass and high electrical conductivity [9, 15]. The valence band engineering and chemical modulation show improvement in the p-d hybridization states in conventional delafossite oxides [21, 22]. The high p-type electrical conductivity mainly originates from the linkage of Cu—O—Cu bonding which can be altered by the group I based delafossite type oxides. In this chapter, we present the ground state properties, lattice dynamical properties and optical properties of $CuMO_2$ (M=H

,Li ,Na,K,Rb) compounds within the framework of density functional theory calculations. The chapter is organized as follows: initially, in Section 4.2, we present computational details, Section 4.3 presents the results and discussion on structural, electronic, dynamical, and optical properties of $CuMO_2$ (M=H ,Li ,Na,K,Rb) compounds and conclusions are presented in Section 4.4.

4.2 Computational Methods

The calculations were performed using a plane wave pseudopotential method based on density functional theory (DFT) [23] implemented in Quantum Espresso code [24]. The generalized gradient approximation (GGA) was used for exchange-correlation functional [25] in which the energy was parameterized by Perdue, Burke, and Ernzerhof (PBE) within norm-conserving pseudopotentials. Following a series of test calculations a plane wave cut-off of 100 Ry and k-point grids of size 10x10x10 in the Monkhorst-pack scheme were adopted [26]. Structural optimization was performed by a constant pressure variable cell using the Parrinello-Rahman method [27]. In all the calculations the convergence value between two consecutive steps was set to 10^{-4} eVÅ^{-1} and 0.001 eVÅ^{-1} for energy and force respectively. The electron-ion parameters of a unit cell were relaxed under Broyden-Fletcher-Goldfarb-Shannon (BFGS) algorithm [28]. Vibrational properties were calculated by employing density functional perturbation theory (DFPT) [29]. The optical properties were determined by Kramers–Kronig transformation (the long wavelength expression for the imaginary part of the dielectric tensor) within the random phase approximation (RPA) for the accurate prediction of absorption spectra [30, 31].

4.3 Results and Discussion

4.3.1 Structural Properties

The $CuHO_2$ possess orthorhombic crystal symmetry with the $Pmn2_1$ $(\#31)$ space group (Fig. 4.1 (a)). This compound contains eight atoms in a unit cell with two non-equivalent oxygen (O) atoms. The two equivalent copper (Cu) atoms and a single hydrogen (H) atom are bonded with the O atoms in a distorted trigonal non-coplanar geometry. The O-H bond length and two equivalent Cu—O bond lengths are 1.04 Å, 1.87 Å, and 1.89 Å respectively. Fig. 4.1(b) presents the crystal geometry of $CuLiO_2$ which crystallizes in the monoclinic structure with the C_2/m $(\#12)$ space group. $CuLiO_2$ contains four atoms in a unit cell arranged in a manner that the single Li atom shares the bond with six equivalent O atoms and edge shared LiO_6 octahedra is created.

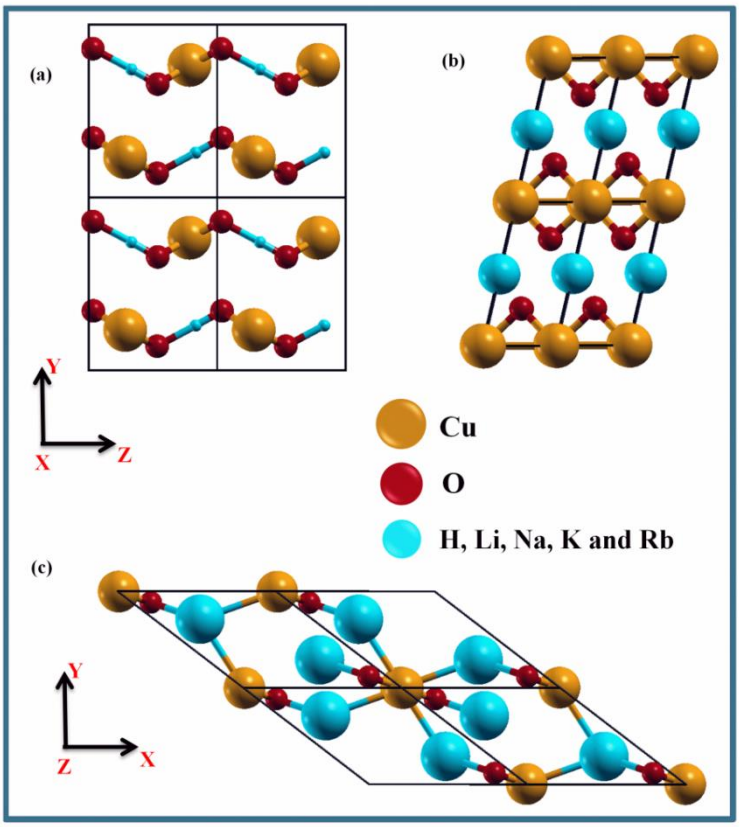

Figure 4.1: Crystal geometry of (a) $CuHO_2$ (b) $CuLiO_2$ and (c) $CuAO_2$ (A= Na, K and Rb).

The bond lengths for the Cu—Li, O—Li and Cu—O are 2.77 Å, 2.15 Å and 1.85 Å respectively. The $CuNaO_2$, $CuKO_2$, and $CuRbO_2$ compounds symmetrize in orthorhombic crystal geometry with $Cmcm$ $(\#63)$ space group (Fig. 4.1(c)). The sodium (Na), potassium (K), and rubidium (Rb) atoms are bounded to six equivalent O atoms and possess eight atoms in a unit cell. Bond length of (Na, K, Rb)—O increases as the radius of alkali atoms increases and Cu-O bond length remains constant in all the five studied compounds. Table 4.1 summarizes the calculated lattice parameters along with previously reported experimental and theoretical data.

Table 4.1: Lattice parameters (a, b, c in Angstrom) of $CuMO_2$ (M=H, Li, Na, K, Rb).

System	a (Å)	b (Å)	c (Å)
$CuHO_2$	2.82	4.42	5.96
$CuLiO_2$	5.78 (5.73)	3.20 (2.71)	5.55 (5.62)
$CuNaO_2$	3.68	11.12	5.44
$CuKO_2$	4.17 (4.37)	11.43 (11.69)	5.51 (5.41)
$CuRbO_2$	4.50 (4.75)	11.97 (11.95)	5.53 (5.40)

Experimental values are shown in brackets.[63,64]

4.3.2 Electronic Band Structure

To understand the inborn electronic properties of $CuMO_2$ (M = H, Li, Na, K, Rb) compounds, the electronic band structure is calculated. The effective mass of electrons and holes and the magnetic moment of an electron can be estimated by electronic band structure. The electronic band structure of $CuMO_2$ (M=H, Li, Na, K, Rb) compounds are presented in Fig. 4.2(a-e). It can be seen from the Fig. 4.2(a-e) that all the nominee compounds possess an indirect energy band gap of 0.5 eV, 0.52 eV, 0.71 eV, 0.86 eV, and 1.0 eV respectively for $CuMO_2$ $(M = H, Li, Na, K, Rb)$. The calculated electronic band structure is presented along the k path of **Γ−X−S−R−Z−Γ** for $CuNaO_2$, $CuKO_2$ and $CuRbO_2$, and **Γ−Y−Z−C−Γ** and **Γ−T−Z−X−U−Y−S−R−Γ** and for $CuLiO_2$ and $CuHO_2$ respectively. The band gap increases as the ionic radii increase i.e. from H to Rb. The orbital contribution of each atom and the nature of the electronic bands can be estimated by the projected density of states (PDOS). The calculated PDOS of $CuMO_2$ (M=H, Li, Na, K, Rb) the compound is presented in Fig. 4.3(a-

e). It can be observed from Fig. 4.3(a-e) that the valence band maximum (VBM) is dominated by Cu 3dand O 2p orbitals in $CuHO_2$, while, orbital H-1s show the least contribution (see Fig. 4.3(a)). The Cu 3ddominates in both conduction band minimum (CBM) as well as in valence band maximum (VBM) for $CuHO_2$.

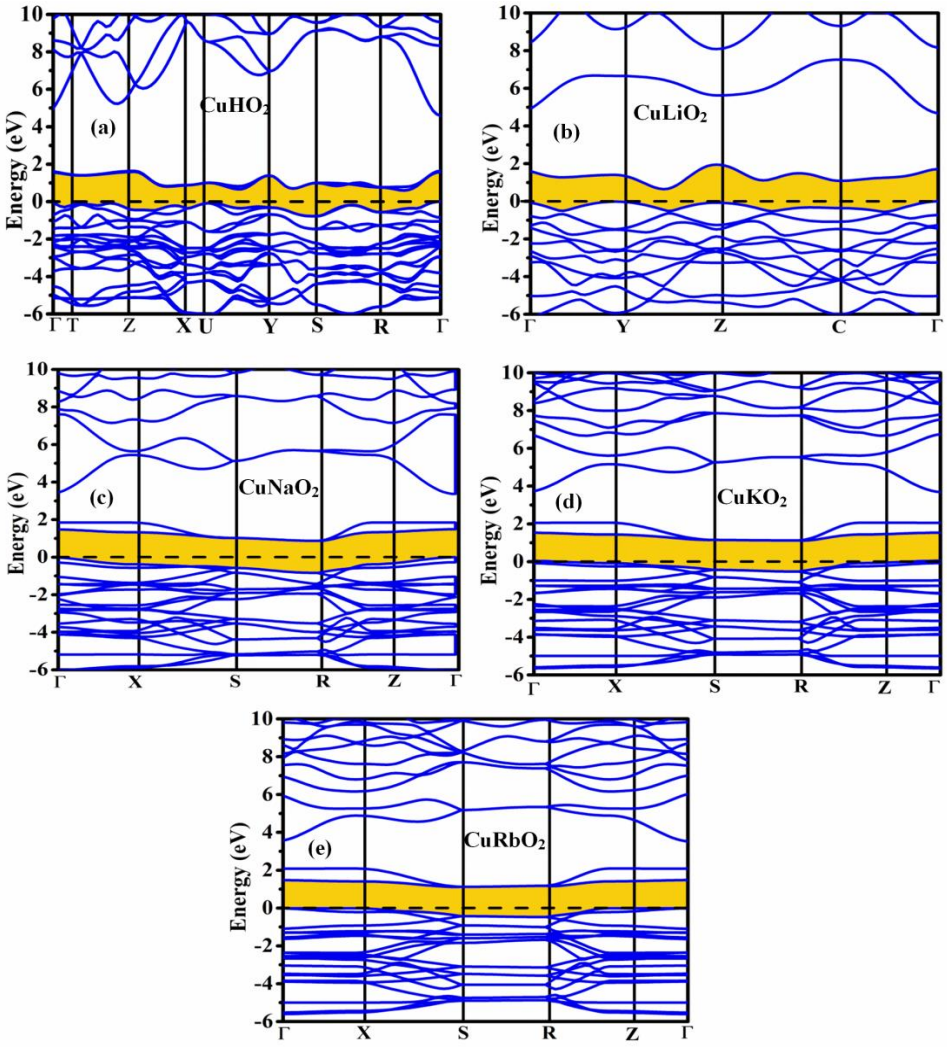

Figure 4.2: Electronic band structure of $CuMO_2$ compounds (a) $CuHO_2$ (b) $CuLiO_2$ (c) $CuNaO_2$ (d) $CuKO_2$ and (e) $CuRbO_2$.

Furthermore, the PDOS shows that the Cu 3dorbital is formed from the equal sub-orbital contributions of d_z^2 and d_{zy}, while, O shows the maximum contribution of p_z. In the case of $CuLiO_2$, the VBM is formed by the equal contribution of Cu 3dand O 2p orbitals. However, the O 2p contribution in $CuLiO_2$ is higher than the $CuHO_2$ in VBM and CBM, suggesting the delocalization of holes.

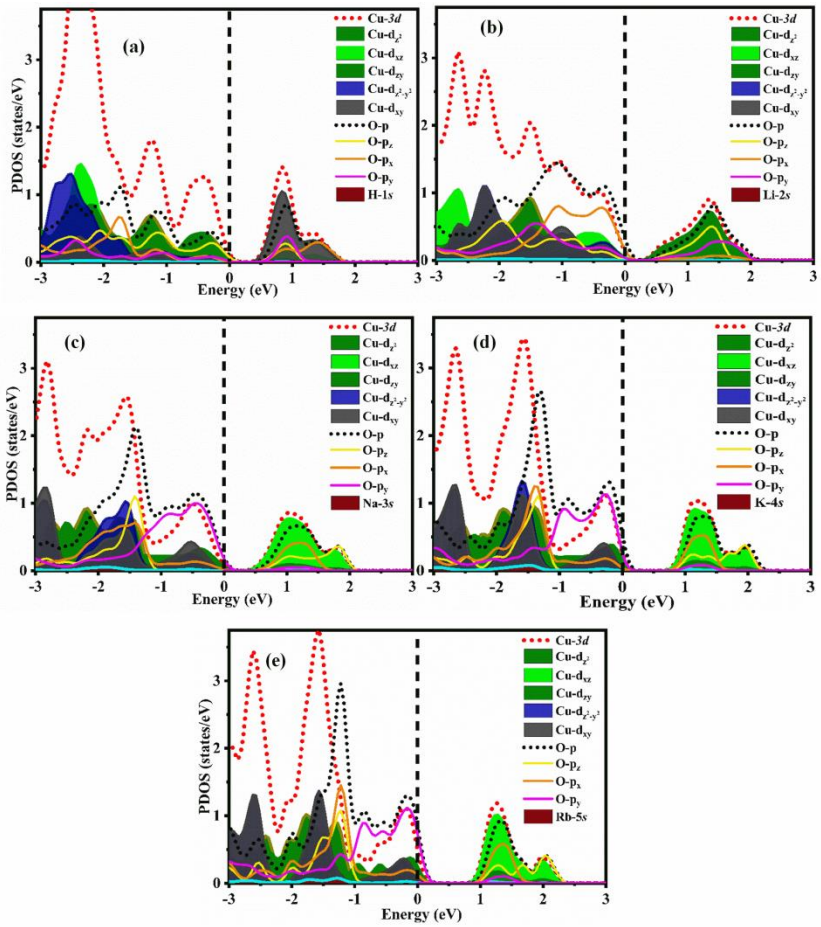

Figure 4.3: Projected density of states (PDOS) of $CuMO_2$ compounds (a) $CuHO_2$ (b) $CuLiO_2$ (c) $CuNaO_2$ (d) $CuKO_2$ and (e) $CuRbO_2$.

The conduction band minimum dominates by Cu 3dand its d_{xz} sub-orbital, while, VBM shows the maximum contribution of O 2p mainly originating from the Op_y orbitals for Na, K, and Rb based $CuMO_2$ delafossites. The contribution of O 2p orbitals increases as we move from *H* to *Rb*. The overlap of Cu-O orbitals which is useful for achieving the high conductivity in p-type oxides is attributed to the enhanced O 2p contribution. The occurrence of holes near the VBM is due to the enhancement of O 2p contribution near the VBM, which requires low energy to migrate to the conduction band. This unusual behavior of O 2p orbital in $CuMO_2$ (M=H, Li, Na, K, Rb) delafossites occur due to the transfer of charge between O 2p and Cu 3d orbitals. From these observations, we can conclude that the p-d hybridization increases as we move from H to Rb of group I in $CuMO_2$ delafossites.

4.3.3 Phonon Dispersion Curves

The knowledge of phonons in a crystal is essential to estimate the lattice dynamical behavior, the atomic vibrations, electron-phonon interaction, thermal conductivity, phase transition and dynamical stability [29, 33-37]. Here, phonon dispersion curves (PDCs) are calculated to understand the behavior of phonons and their role in dynamical stability. Figure 4.4(a-e) represents the PDCs along with the phonon density of states (PhDOS) for the $CuMO_2$ (M=H, Li, Na, K, Rb) compounds. The absence of imaginary frequencies that can be seen from Fig. 4.4(a-e) indicates the dynamical stability of these $CuMO_2$ (M=H, Li, Na, K, Rb) compounds. Except for $CuLiO_2$, all the compounds in group I based delafossites possess eight atoms in the unit cell results in the 24 phonon branches with 21 optical and three acoustic modes. Nevertheless, $CuLiO_2$ which possesses four atoms in the unit cell results in twelve phonon branches. Based on their point group symmetry, now we turn our attention towards the phonon behavior of $CuMO_2$ (M=H, Li, Na, K, Rb) compounds. The character table of these compounds is shown in Table 4.2 and 4.3. Furthermore, three different space groups are associated with the $CuMO_2$, hence, we present the details of phonons one by one. The first element of group I i.e. H in $CuMO_2$ belongs to the C_{2v} point group symmetry. The group theoretical analysis of $CuHO_2$ yields the following irreducible representations at the zone center [38].

$$\Gamma = 2A_1 + A_2 + B_1 + 2B_2 \quad (4.1)$$

The PDCs of $CuHO_2$ is separated into three regions, due to the O-Cu-O vibrations the middle region in PDC shows less dispersive behavior and that reflects the intense peak in PhDOS. In $CuHO_2$, the highest frequency of 2500 cm^{-1} appears due to the O-H vibration. We found the same O-H vibrations in formerly reported $HCoO_2$ delafossite [39]. The PDCs for $CuLiO_2$ are highly dispersed in nature and equally distributed in the whole region (see Fig. 4.4 (b)).

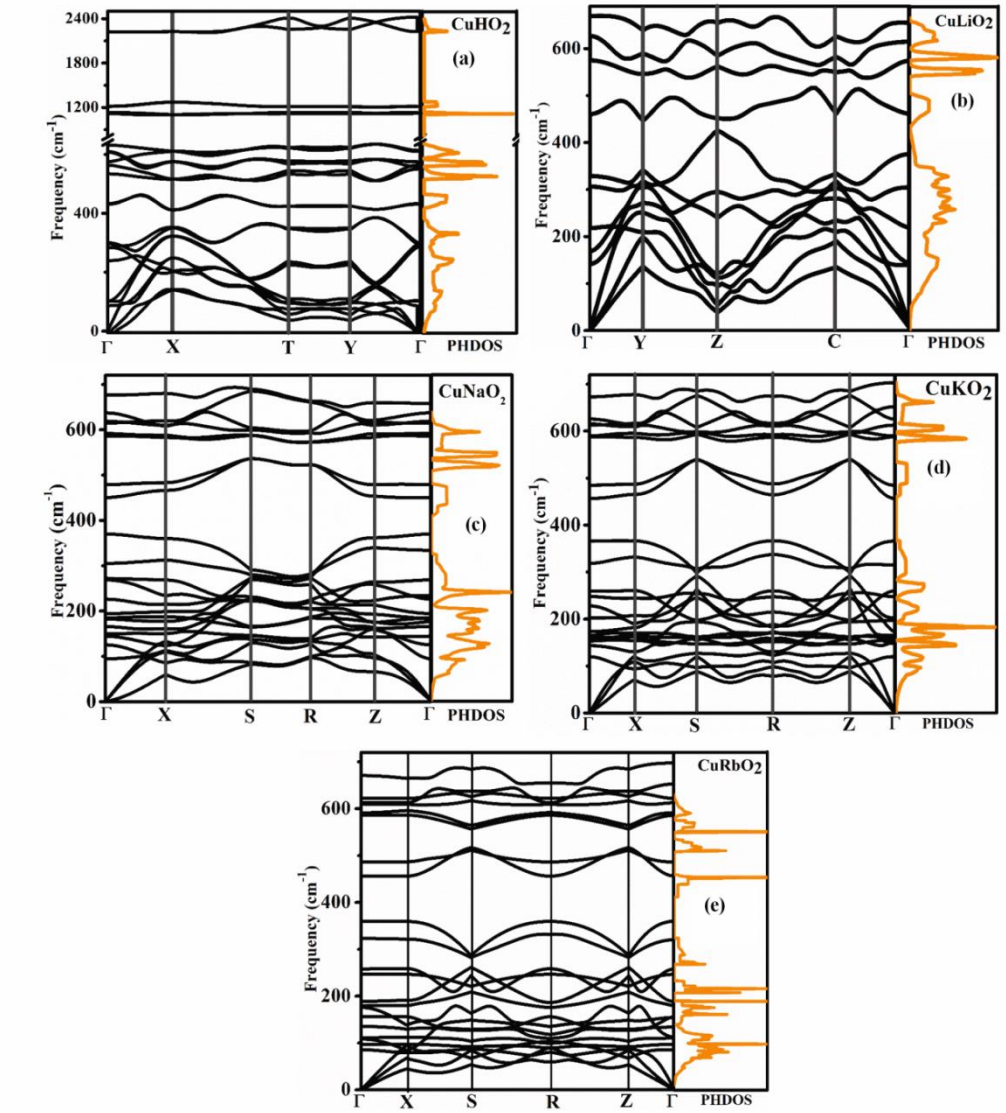

Figure 4.4: The phonon dispersion curves of (a) $CuHO_2$ (b) $CuLiO_2$ (c) $CuNaO_2$ (d) $CuKO_2$ and (e) $CuRbO_2$.

The C_{2h} point group symmetry and space group analysis shows following irreducible representation at the zone center:

$$\Gamma = 3A_u + 6B_u + 2A_g + B_g \tag{4.2}$$

where u and g represent IR and Raman active modes respectively.

Table 4.2: Character Table of $CuHO_2$ and $CuLiO_2$

$C_{2v}(mm2)$	E	2z	m_y	m_x	Functions	$C_{2h}(2/m)$	E	2	-1	m	functions
A_1	1	1	1	1	z, x^2, y^2, z^2	A_g	1	1	1	1	z, x^2, y^2, z^2, xy, jz
A_2	1	1	-1	-1	xy, j_z	B_g	1	-1	1	-1	$xy, yz, j_x\, j_y$
B_1	2	-1	1	-1	x, xz, j_y	A_u	2	1	-1	-1	z
B_2	1	-1	-1	1	y, y_z, j_x	B_u	1	-1	-1	1	x, y

Table 4.3: Character table of $CuNaO_2$, $CuKO_2$ and $CuRbO_2$

D_{2h} (mmm)	E	2_z	2_y	2_x	-1	m_z	m_y	m_x	Functions
A_g	1	1	1	1	1	1	1	1	x^2, y^2, z^2
B_{1g}	1	1	-1	-1	1	1	-1	-1	xy, J_z
B_{2g}	1	-1	1	-1	1	-1	1	-1	xz, J_y
B_{3g}	1	-1	-1	1	1	-1	-1	1	yz, J_x
A_u	1	1	1	1	-1	-1	-1	-1	-
B_{1u}	1	1	-1	-1	-1	-1	1	1	z
B_{2u}	1	-1	1	-1	-1	1	-1	1	y
B_{3u}	1	-1	-1	1	-1	1	1	-1	x

The third, fourth and fifth elements of group I i.e. Na, K, and Rb of $CuMO_2$ delafossite possess D_{2h} point group symmetry and their PDCs are presented in Fig. 4.4(c-e). Additionally, the $CuNaO_2$, $CuKO_2$ and $CuRbO_2$ compounds belong to the $Cmcm$ space group. The group theory analysis of the space group of these compounds gives the following irreducible representation at the zone center :

$$\Gamma = 3A_g + 2B_{1g} + 3B_{1u} + 3B_{2u} + 3B_{3g} + 2B_{3u} + B_{2g} + A_u \quad (4.3)$$

There is a small difference in dispersion curves while a similar frequency range is observed for $CuNaO_2$**,** $CuKO_2$ and $CuRbO_2$ compounds. The highest optical branches are separated as we go from Na to K to Rb due to the (Na, K, Rb)-O vibrations. The increase in ionic radii increases (Na, K, Rb)-O bond length which results in the separation of optical branches. In the middle region optical branches are separated near 300-350 cm^{-1} due to an increment in the bond length of (Na, K, Rb)-Cu as we move from Na to Rb. Table 4.4 shows the Born effective charge tensors (Z^*) for $CuMO_2$ (M= H, Li, Na, K, Rb) compounds and can be attributed to the lattice vibrations and the LO-TO splitting, which describes the change in electronic polarization with the ionic displacements. The larger value of the Born effective charges indicates the larger LO–TO splitting in combination with the smaller values of the dielectric tensor components. The Born effective charge tensors are anisotropic with non-negligible diagonal elements for the $CuMO_2$ compound. Moreover, these charges are sensitive to the structural details and in a cubic environment, they are diagonal and isotropic. However, non-cubic and complex systems

illustrate anisotropic behavior [40]. For $CuHO_2$ and $CuLiO_2$, diagonal components of Born effective charges are different due to the different structural parameters in these two oxides. While in $CuNaO_2$, $CuKO_2$ and $CuRbO_2$, the effective charges are found largest and effective charge tensors are similar in each system.

Table 4.4: Born effective charges Z^* in atomic units of $CuMO_2$ (M=H ,Li ,Na,K,Rb)

	$CuHO_2$	$CuLiO_2$	$CuNaO_2$	$CuKO_2$	$CuRbO_2$
Z^*_{Cu}	4.17 0.0 0.15 0.0 0.81 0.16 0.0 0.15 0.61	1.49 1.18 0.06 1.18 3.48 −0.02 −0.32 0.15 0.64	0.62 −0.08 0.0 − 0.08 0.38 0.0 0.0 0.0 3.87	0.55 −0.10 0.0 −0.10 0.32 0.0 0.0 0.0 3.96	0.52 −0.12 0.0 −0.12 0.26 0.0 0.0 0.0 4.02
Z^*_{M}	0.16 0.0 0.0 0.0 2.39 1.16 0.0 0.01 0.33	1.15 0.04 −0.15 0.04 1.23 0.07 −0.26 0.12 1.72	1.43 −0.13 0.0 −0.13 1.07 0.0 0.0 0.0 1.02	1.28 −0.11 0.0 −0.11 1.03 0.0 0.0 0.0 0.88	1.22 −0.07 0.0 −0.09 1.04 0.0 0.0 0.0 0.91
Z^*_{O1}	−2.0 0.0 0.0 0.0 −1.72 −0.42 0.0 0.21 −0.57	− 1.33 −0.61 0.04 − 0.61 −2.36 −0.02 0.29 −0.13 −1.18	− 1.03 0.11 −0.0 0.11 −0.72 0.0 −0.08 0.02 −2.44	−0.92 0.11 0.00 0.11 −0.67 0.00 −0.05 0.02 −2.42	−0.90 0.11 0.01 0.11 −0.66 0.00 −0.03 0.01 −2.47
Z^*_{O2}	−2.01 0.0 0.0 0.0 −1.48 0.81 0.0 −0.14 −0.37	− 1.33 −0.61 0.04 − 0.61 −2.36 −0.02 0.29 −0.13 −1.18	− 1.03 0.11 −0.0 0.11 −0.72 0.0 0.08 0.02 −2.44	−0.92 0.11 −0.00 0.11 −0.67 0.00 −0.05 −0.02 −2.42	−0.90 0.11 −0.01 0.11 −0.66 0.00 −0.03 −0.01 −2.47

4.3.4 Optical Properties

Due to robust p–d hybridization and wide range of band gap available through the electronic band structure, it is noteworthy to calculate the optical properties of $CuMO_2$ (M=H, Li, Na, K, Rb) compounds. These properties can provide fruitful applications in optoelectronic devices and helps to understand the interaction of light with the systems.

A. Dielectric Constants

It is well understood that the optical properties of a system can be calculated by the complex dielectric function (CDF). The Kramer–Kroning transformation within the random phase approximation (RPA) is used to calculate the real part (ε_1 (ω)) of the dielectric function. Other pivotal optical parameters can be expressed from the CDF. The CDF is used to calculate optical parameters and can be derived by measuring the linear response to an external electromagnetic field with a small wave vector *k* [41-42].

Expressions for the absorption coefficient, refractive index, coefficient of extinction, optical reflectivity and loss spectra are given as follows:

$$\varepsilon(\omega) = \varepsilon_1(\omega) + i\,\varepsilon_2(\omega) \tag{4.4}$$

The electronic band structure through the momentum matrix element and the joint density of states (JDOS) between the unoccupied and occupied wave functions within the selection rules, is used to determine the imaginary part ($\varepsilon_2(\omega)$) of the dielectric function and given by:

$$\varepsilon_2(\omega) = \frac{2e^2\pi}{\Omega\,\varepsilon_0}\sum_{k,c,v}\int |\psi_k^c < \hat{u}\times \mathrm{r} > \psi_k^v|^2\,\delta(\mathrm{E}_k^c - \mathrm{E}_k^v - E) \tag{4.5}$$

$$\varepsilon_1(\omega) = 1 + \frac{2}{\pi}P\int \frac{\omega'\varepsilon_2(\omega')}{\omega'^2-\omega^2}d\omega' \tag{4.6}$$

The above equation depicts the involvement of valence and conduction bands i.e. JDOS and momentum matrix element. The Kramer–Kronig relation is used to calculate $\varepsilon_1(\omega)$ from $\varepsilon_2(\omega)$ of the dielectric function [43]. The absorption coefficient $\alpha(\omega)$ is obtained directly from the dielectric function $\varepsilon(\omega)$,

$$\alpha(\omega) = \frac{\sqrt{2\omega}}{c}\left[\sqrt{(\varepsilon_1^{\,2} + \varepsilon_2^{\,2} - \varepsilon_1}\right]^{\frac{1}{2}} = \alpha = \frac{2\omega k}{c} = \frac{4\pi k}{\lambda_0} \tag{4.7}$$

where c is the speed of light. As mentioned above, all other optical parameters can be calculated by the Equations (4.5) and (4.6).

$$k(\omega) = \frac{1}{\sqrt{2}}\left[(\varepsilon_1^{\,2} + \varepsilon_2^{\,2})^{\frac{1}{2}} - \varepsilon_1\right]^{1/2} \tag{4.8}$$

$$n(\omega) = \frac{1}{\sqrt{2}}\left[(\varepsilon_1^{\,2} + \varepsilon_2^{\,2})^{\frac{1}{2}} + \varepsilon_1\right]^{1/2} \tag{4.9}$$

$k(\omega)$ and $n(\omega)$ represent the extinction coefficient and refractive index respectively in Equations (4.8) and (4.9). The Equation (10) is used to determine the reflectivity($R(\omega)$), and given by

$$R(\omega) = \frac{[(n-1)^2+k^2]}{[(n+1)^2+k^2]} \tag{4.10}$$

Now, to calculate the energy loss by an electron in the semiconductors, we have calculated the loss function $L(\omega)$, which is given by

$$L(\omega) = \frac{\varepsilon_2(\omega)}{\varepsilon_1^2(\omega)+\varepsilon_2^2(\omega)} \tag{4.11}$$

All optical properties can be calculated by $\varepsilon_1(\omega)$ and $\varepsilon_2(\omega)$ the dielectric function.

B. Real Part $\varepsilon_1(\omega)$ and Imaginary Part $\varepsilon_2(\omega)$ of the Dielectric Function

Figure. 4.5(a-e) represent the complex dielectric functions of $CuMO_2$ (M=H, Li, Na, K, Rb) compounds. The similar behavior of $\varepsilon_1(\omega)$ is found for all the considered compounds except for $CuLiO_2$ (see Fig. 4.5 (b)), due to the dissimilarity in the structural feature (see Fig. 4.1). It can be seen from Fig 4.5(a-e) that the real part of the dielectric function $\varepsilon_1(\omega)$ reaches minima at higher energy values and maxima at lower energy values. The peak intensity of $\varepsilon_1(\omega)$ increases at the higher energy side, which can be attributed to the increment in the electronic band gap as we move from $H \rightarrow Li \rightarrow Na \rightarrow K \rightarrow Rb$. However, these intense peaks arise due to the electronic transition between the bottom of the conduction band and the top of the valence band.

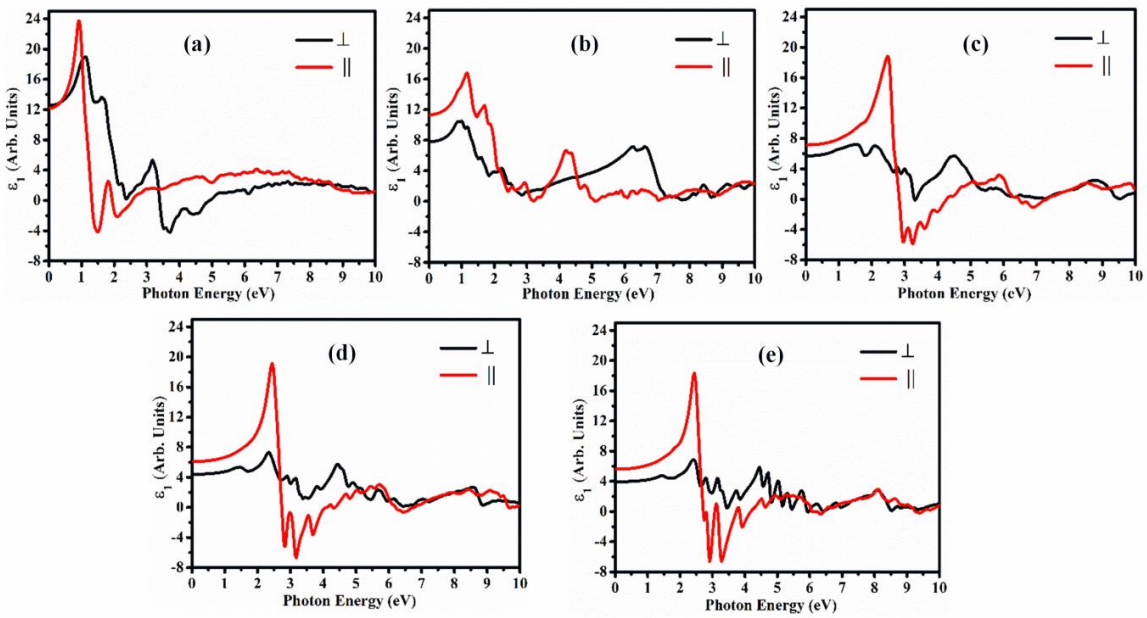

Figure 4.5: Real part of a dielectric function of (a) $CuHO_2$ (b) $CuLiO_2$ (c) $CuNaO_2$ (d) $CuKO_2$ and (e) $CuRbO_2$.

Table 4.5: Static (ε_0) and high frequency (ε_∞) dielectric constant in parallel and perpendicular directions, dielectric tensor ($\Delta\varepsilon_0$) along with refractive index n(0) and degree of birefringence $\Delta n(0)$ of $CuMO_2$ (M=H, Li, Na, K, Rb).

Compounds	$\varepsilon_0 \perp \boldsymbol{c}$	$\varepsilon_0 \parallel \boldsymbol{c}$	$\varepsilon_\infty \perp \boldsymbol{c}$	$\varepsilon_\infty \parallel \boldsymbol{c}$	ε_0	$\Delta\varepsilon_0$	$\boldsymbol{n(0)} \perp \boldsymbol{c}$	$\boldsymbol{n(0)} \parallel \boldsymbol{c}$	$\boldsymbol{n(0)}$	$\Delta\boldsymbol{n(0)}$
$CuHO_2$	12.53	12.18	12.39	8.40	12.38	-0.028	3.54	3.51	3.52	-0.03
$CuLiO_2$	7.7	11.29	5.023	9.32	10.01	0.35	2.81	3.38	3.09	0.57
$CuNaO_2$	5.67	7.05	3.63	5.11	5.98	0.23	2.39	2.66	2.52	0.27
$CuKO_2$	4.46	6.03	2.65	4.30	4.73	0.33	2.09	2.46	2.28	0.37
$CuRbO_2$	3.88	5.57	2.50	4.06	4.28	0.39	1.99	2.37	2.17	0.38

The parallel and perpendicular components to c-axis, static part of a dielectric constant ($\varepsilon_1(0)$) and the average between them along with the differences i.e. $\Delta\varepsilon$ is shown in Table 4.5. The static dielectric constants are 12.50, 7.74, 5.71, 4.28, and 3.90 for $CuHO_2$, $CuLiO_2$, $CuNaO_2$, $CuKO_2$, and $CuRbO_2$ respectively. The above values suggest that the smaller band gap gives a larger $\varepsilon_1(0)$, representing to Penn's model [44]. The boron, aluminum, gallium, rhodium, and indium based chalcopyrites ($CuMX_2$; M= Ga, Al, In, B, Rh; X= S, Se, Te) show $\varepsilon_1(0)$ *the* value within the range of 8.20–12.91 and for traditional delafossites i.e. $CuAlO_2$, it is 2.108 [45-52]. Furthermore, the calculated $\varepsilon_1(0)$ value for earlier studied conventional delafossites ABO_2 (A= Cu, Ag; B= Al, Ga, In) lie within the range of 7.2–10.2 [53]. These calculated values of static dielectric constants nominate $CuHO_2$ and $CuLiO_2$ as high dielectric constant materials and can be used in optoelectronic devices such as epitaxial and capacitor dielectrics, whereas, $CuNaO_2$, $CuKO_2$ and $CuRbO_2$ are categorized as low dielectric constant materials [51]. Figure 4.6 (a-e)) represents calculated imaginary part of a dielectric constant $\varepsilon_2(\omega)$ for the $CuMO_2$ (M=H, Li, Na, K, Rb) compounds corresponding to the photon energy up to 10 eV. The behavior of $\varepsilon_2(\omega)$ is linked to the electronic band structure of the $CuMO_2$ compound. The $CuHO_2$ and $CuLiO_2$ compounds show distinct line shapes of $\varepsilon_2(\omega)$, because of their distinctions in the electronic band structure, while, nearly same line shapes of $\varepsilon_2(\omega)$ for $CuNaO_2$, $CuKO_2$, and $CuRbO_2$ are observed and attributed to the similar nature of the electronic band structure.

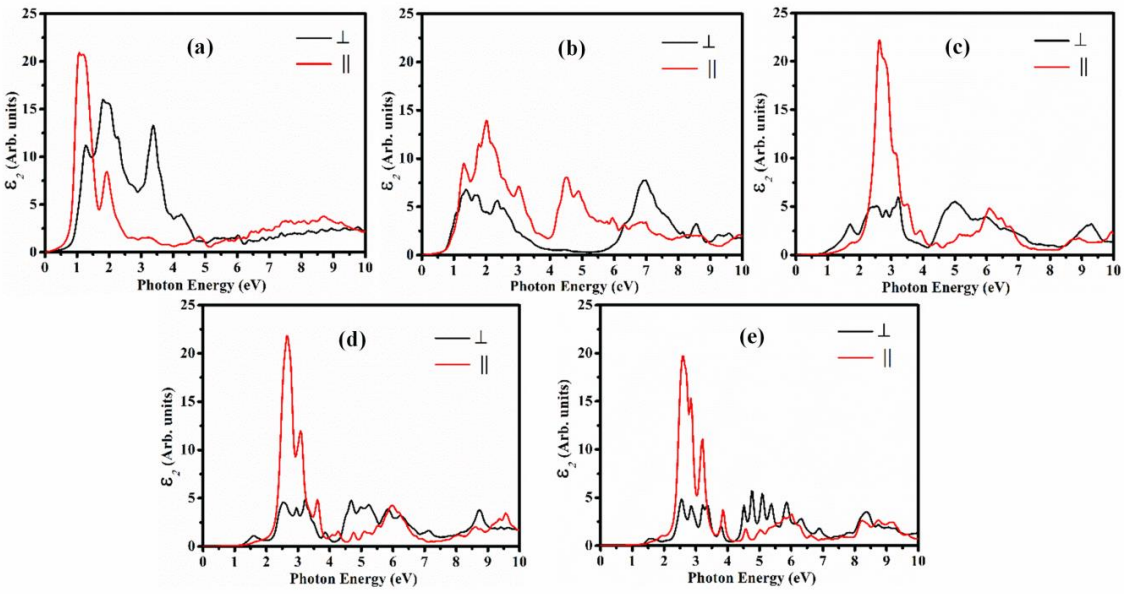

Figure 4.6: Imaginary part of a dielectric function of (a) $CuHO_2$ (b) $CuLiO_2$ (c) $CuNaO_2$ (d) $CuKO_2$ and (e) $CuRbO_2$.

The hybridized bonding between Cu 3d and O 2p orbitals are responsible for these sharp peaks in $\varepsilon_2(\omega)$ for all $CuMO_2$ compounds. The threshold occurs at 0.44 eV, 0.75 eV, 0.86 eV, 1.2 eV, and 1.3 eV for $CuHO_2$, $CuLiO_2$, $CuNaO_2$, $CuKO_2$, and $CuRbO_2$ respectively. They are attributed to the band gap of the scrutinized compounds, signifying the expected output of the $\varepsilon_2(\omega)$ from the electronic band structure. The various interband electronic transitions are associated with the imaginary part of the dielectric function and the threshold of absorption occurs due to the direct electronic transition from the top of the valence band to the bottom of the conduction band. The behavior of the studied compounds resembles the formerly studied traditional delafossites [45-53].

C. Absorption Coefficient $\boldsymbol{\alpha(\omega)}$

The possibilities of $CuMO_2$ (M=H, Li, Na, K, Rb) compounds for photovoltaic conversion application, we have studied absorption spectrum corresponding to photon energy up to 5 eV and presented them in the panels of Figs. 4.7(a-e). The threshold of absorption occurs at 0.85 eV, 0.90 eV, 1.48 eV, 1.76 eV and 1.8 eV for $CuHO_2$, $CuLiO_2$, and $CuNaO_2$, $CuKO_2$, $CuRbO_2$ respectively. The $CuHO_2$ and $CuLiO_2$ compounds indicate a maximum peak in the ultraviolet

region (see Figs. 4.7(a-b)), indicating the utility of these compounds for optoelectronics in the higher energy region, whereas, in the visible region, $CuNaO_2$, $CuKO_2$, and $CuRbO_2$ show maximum peak (see Figs. 4.7(c-e)), suggesting the usefulness of these compounds in photovoltaic conversion applications.

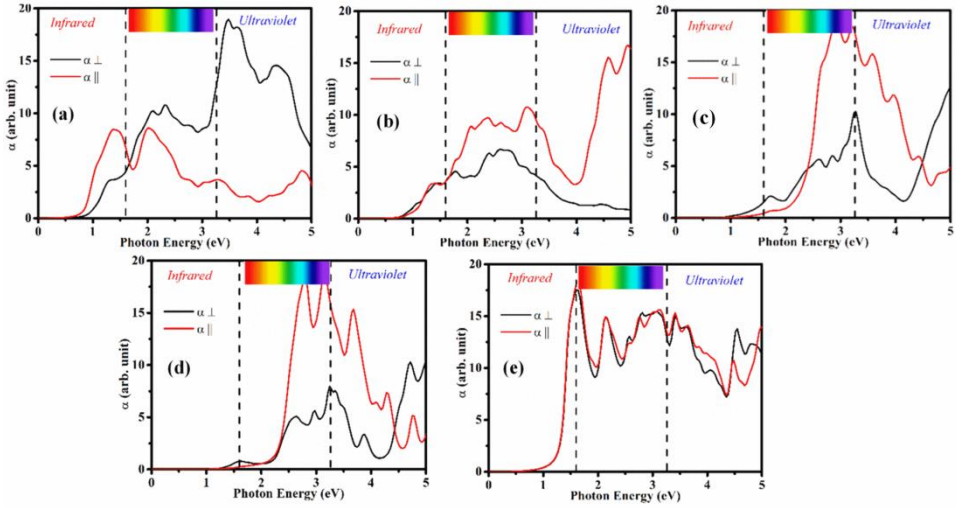

Figure 4.7: Absorption coefficient of (a) $CuHO_2$ (b) $CuLiO_2$ (c) $CuNaO_2$ (d) $CuKO_2$ and (e) $CuRbO_2$.

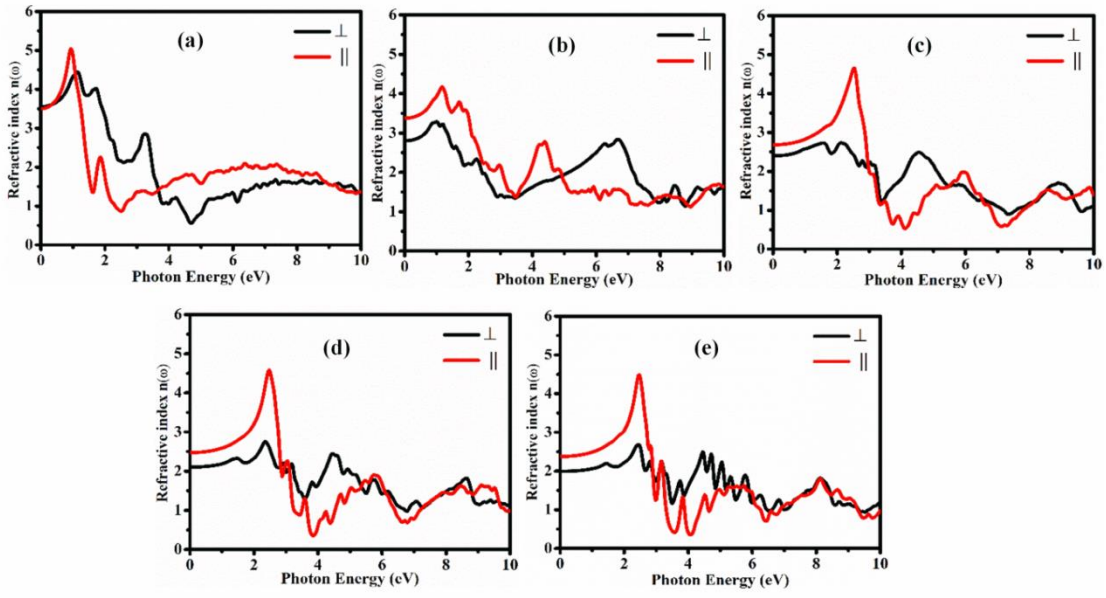

Figure 4.8: Refractive index of (a) $CuHO_2$ (b) $CuLiO_2$ (c) $CuNaO_2$ (d) $CuKO_2$ and (e) $CuRbO_2$.

These fundamental absorption edge values are comparable with the nitride based delafossites ABN_2 (A = Cu, Ag, Au; B = V, Nb, Ta) [54]. The other traditional delafossites such as $CuAlO_2$, ABO_2 (A= Cu, Ag; B= Ga, Al, In), $AgAlO_2$, $AgCrO_2$, and $AgScO_2$ reveal the

fundamental absorption edge within the range of 0.5–5 eV [53, 55-57]. According to the Shockley Queisser efficiency model, $CuNaO_2$, $CuKO_2$ and $CuRbO_2$ compounds are very close to the optimal band gap, thus can be used as a solar absorber, while, $CuHO_2$ and $CuLiO_2$ can be used in the optoelectronic applications [58].

D. Refractive index $\boldsymbol{n(\omega)}$ and Extinction Coefficient $\boldsymbol{k(\omega)}$

To understand the utility of these compounds in the optoelectronics, we have calculated the refractive index of these compounds and presented them in Fig. 4.8(a-e). To analyze the polarization of the compounds the refractive index is calculated. Table 4.5 represents the calculated values of refractive index and are given by 3.55, 2.80, 2.40, 2.11 and 1.98 for $CuHO_2$, $CuLiO_2$, $CuNaO_2$, $CuKO_2$ and $CuRbO_2$ respectively. The parallel and perpendicular components shift towards the higher energy side as we move from H→Li→Na→K→Rb (see Fig. 4.8(a-e)). The refractive index $n(\omega)$ is comparable with previously reported for delafossites such as $CuScO_2$, $CuAlO_2$, and $CuInO_2$ [59-61]. These values of refractive index perpendicular to the c-axis are within the range of 1.98–3.55 and increases as ionic radii increase. The small difference in the values of the refractive index can be directly correlated to the small difference in the ionic radii of Li, Na, K, and Rb. The smaller ionic radii result in the larger refractive index for $CuHO_2$. The refractive index n(ω) increases in the infrared region with a notable sharp peak in the visible region. The birefringence can be calculated by the difference in the parallel and perpendicular refractive indices ($\Delta n = n^{\parallel} - n^{\perp}$). Table 4.5 shows the birefringence values for the group I based delafossites in which $\Delta n(0)$ is positive for all scrutinized compounds except for $CuHO_2$, signifying their potential applications in non-linear optical devices. Figure 4.9(a-e) presents the extinction coefficient $k(\omega)$. The extinction coefficient shows how the oscillation amplitude of the electric field decays with respect to the incident photon energy. The parallel and perpendicular components of $k(\omega)$ for all the

compounds have almost similar nature except for $CuLiO_2$ owing to the difference in the structural as well as electronic properties.

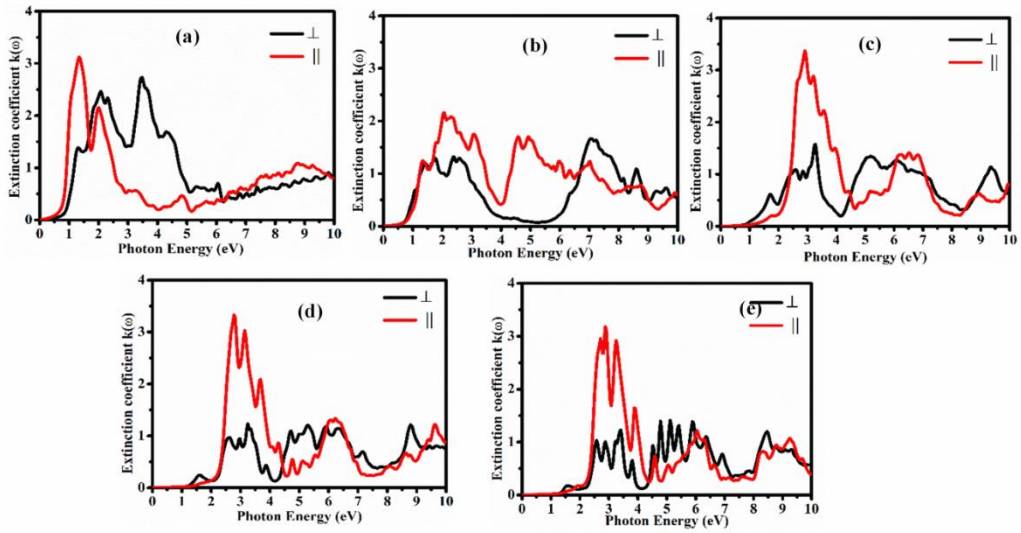

Figure 4.9: Extinction coefficient of (a) $CuHO_2$ (b) $CuLiO_2$ (c) $CuNaO_2$ (d) $CuKO_2$ and (e) $CuRbO_2$.

The small ionic radii contribute more to the coefficients of the extinction spectra. As a result, $CuHO_2$ possesses a more intense peak in the perpendicular direction compared to the scrutinized delafossites such as $CuLiO_2$, $CuNaO_2$, $CuKO_2$, and $CuRbO_2$. The peak intensity in $k(\omega)$ spectra not only shifts towards the higher energy side but also decreases in magnitude as we move from H→Li→Na→K→Rb. Further, an increase in the photon energy increases the magnitude of $k(\omega)$. In the higher energy region, the coefficient of extinction decreases indicating decay of oscillation amplitude of the electric field.

E. Optical Reflectivity $\boldsymbol{R(\omega)}$ and Loss Spectrum $\boldsymbol{L(\omega)}$

Figure 4.10(a-e) represent the optical reflectivity of $CuMO_2$ $(M = H, Li, Na, K, Rb)$ along with the parallel and perpendicular components of polarization. All the reflectivity spectra start with the zero frequency limit, known as static part of reflectivity.

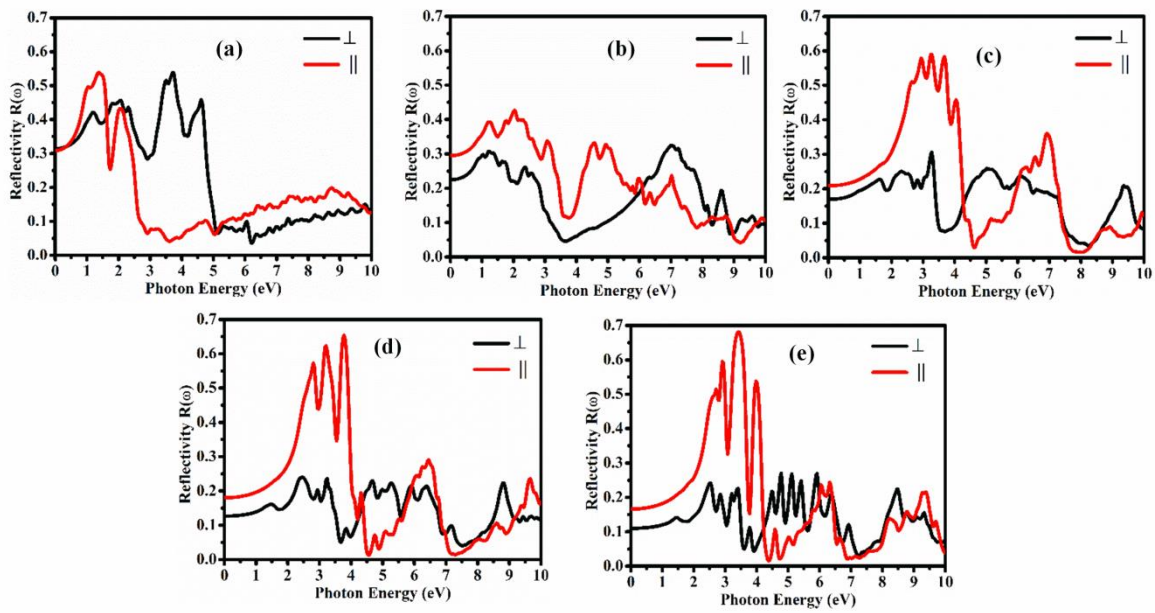

Figure 4.10: Reflectivity spectrum of (a) $CuHO_2$ (b) $CuLiO_2$ (c) $CuNaO_2$ (d) $CuKO_2$ and (e) $CuRbO_2$..

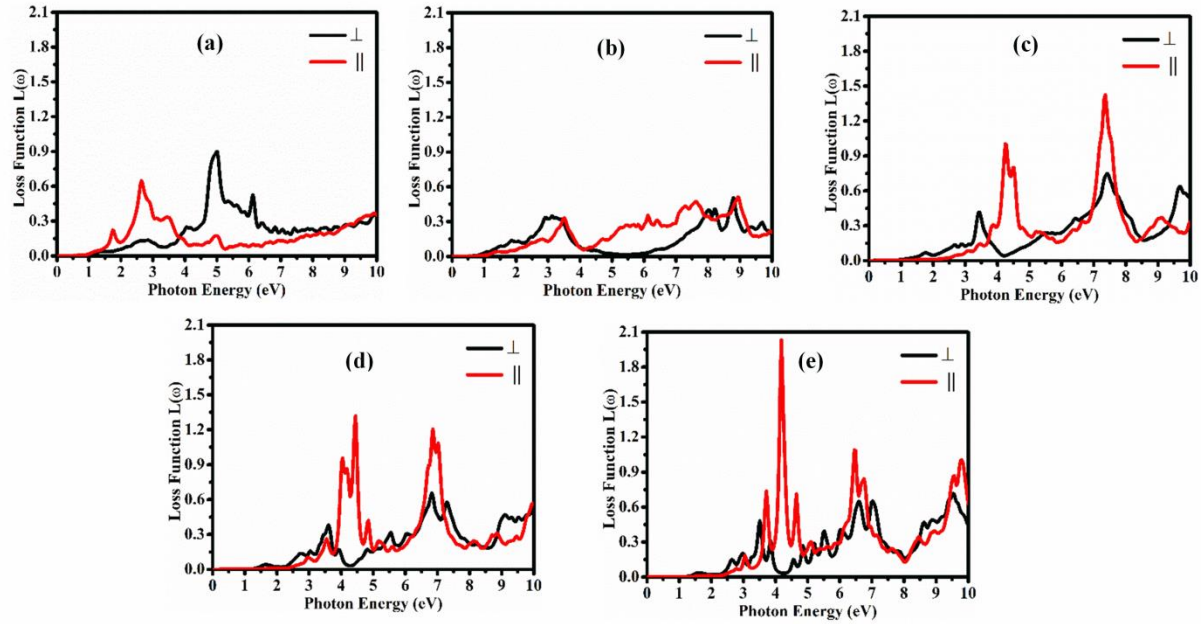

Figure 4.11: Loss Spectrum of (a) $CuHO_2$ (b) $CuLiO_2$ (c) $CuNaO_2$ (d) $CuKO_2$ and (e) $CuRbO_2$.

Furthermore, these spectra increase in the infrared region and decrease in the higher region and achieve the maximum in the visible region. With the change in group I atoms from H to Rb, one can see an increment in the reflectivity at higher energy. This increment can be associated with the increase in the band gap by changing M cation. The increase in the ionic radii of group-I atoms increases the magnitude of the peak in the reflectivity spectra. The optical reflectivity

of $CuMO_2$ is reasonable in the ultraviolet region and maximum in the visible region, indicating the applicability of these compounds as non-linear optical devices and Bragg reflectors [62]. Figure 4.11(a-e) displays the loss of energy by an electron when passing through a homogeneous dielectric medium known as energy loss spectra corresponding to the photon energy up to 10 eV. The larger ionic radii increase the peak intensity in the energy loss spectra,i.e.m H→Rb except for $CuLiO_2$. The main peak in loss spectra is attributed to the bulk plasma oscillation frequency ω_p, which is a collective exciton where the energy levels are unoccupied. A broad plasma peak is associated with the robust hybridization between Cu 3d and O 2p orbitals (Figs. 4.11(a-e)), however, the nature of the loss spectrum for $CuLiO_2$ is different due to the difference in the electronic band structure (see Figs. 4.2(a-e)). $CuNaO_2$, $CuKO_2$, and $CuRbO_2$ compounds display two intense peaks, signifying a rapid loss of energy by an electron in the high-frequency region. These intense peaks can be interrelated to the atomic radii of $CuMO_2$. The small amount of energy loss by an electron in the lower energy region signifies the applicability of these compounds in optoelectronic applications.

4.4 Conclusions

We have examined the ground state properties, lattice dynamical and optical properties of the group I based $CuMO_2$ $(M = H, Li, Na, K, Rb)$ delafossites with an indirect band gap nature. $CuMO_2$ compound possesses low band gap than the traditional delafossites. The p-type conductivity is achieved through the exceptional structural geometry and significant p-d hybridization due to the different bonding nature. The group I based delafossites induce metal-oxygen $(Cu—O)$ overlap due to an increase in the band gap and p-d hybridization as we move from H to Rb. Dynamical stability of the $CuMO_2$ (M=H ,Li ,Na,K,Rb) compounds is confirmed through the phonon dispersion curves and phonon density of states. The absorption coefficient and dielectric constants of $CuMO_2$ indicate that $CuNaO_2$, $CuKO_2$ and$CuRbO_2$ can be used for

solar energy converters. The values of static refractive index, reflectivity spectra and loss spectra indicate the utility of these compounds in optoelectronic applications.

References

1. A. N. Banerjee and K. K. Chattopadhyay, *Prog. Cryst. Growth Charact. Mater*. **50**, 52 (2005).
2. R. G. Gordon, *MRS Bull*. **25**, 52 (2000).
3. X. Yu, T. J. Marks, A. Facchetti, *Nat. Matter*. **15**, 383 (2016).
4. A. Walsh, J. L. F. Da Silva, S. H. Wei, C. Körber, A. Klein, L. F. J. Piper, A. DeMasi, K. E. Smith, G. Panaccione, P. Torelli, D. J. Payne, A. Bourlange, R. G. Egdell, *Phys. Rev. Lett*. **100,** 167402 (2008).
5. S. Lany , A. Zunger, *Phys. Rev. Lett.* **98**, 045501 (2007).
6. K. G. Godinho, A. Walsh, and G. W. Watson, *J. Phys. Chem.* C. **113,** 439 (2009).
7. B. Mohanty, K. K. Naik, S. Sahoo, B. Jena, B. Chakraborty, C. S. Rout, B. K. Jena, *Chemistry Select*. **3**, 9008 (2018).
8. H. Kawazoe, M. Yasukawa, H. Hyodo, M. Kurita, H. Yanagi, H. Hosono, *Nature.* **389**, 939 (1997).
9. E. Fortunato, P. Barquinha, R. Martins, *Adv. Mater.* **24,** 2945 (2012).
10. S. Fraga, S. Karwowski, K.M.S. Saxena, Handbook of Atomic Data, Elsevier, Amsterdam, (1976).
11. B. A. D. Williamson, J. Buckeridge, J. Brown, S. Ansbro, R. G. Palgrave, D. O. Scanlon, *Chem. Mater*. **29**, 2432 (2017).
12. H. Kawazoe, H. Yanagi, K. Ueda, H. Hosono, *MRS Bull*. **25,** 28 (2000).
13. R. Nagarajan, A. Draeseke, A. Sleight and J. Tate, *J. Appl. Phys*. **89,** 8022 (2001).
14. G. Hautier, A. Miglio, G. Ceder, G. M. Rignanese and X. Gonze, *Nat. Commun.* **4,** 2292 (2013).
15. T. F. Cerqueira, S. Lin, M. Amsler, S. Goedecker, S. Botti, M. A. Marques, *Chem. Mater.* **27**, 4562 (2015).
16. J. Shi, T. F. T. Cerqueira, W. Cui, F. Nogueira, S. Botti, A. A. L. Marques, *Sci. Rep*. **7**, 43179 (2017).
17. R. Nagarajan, N. Duan, M. K. Jayaraj, J. Li, K. A. Vanaja, A. Yokochi, A. Draeseke, J. Tate, A. W. Sleight, *Int. J. Inorg. Mater.* **3,** 265, (2001).
18. D. O. Scanlon, G. W. Watson, *J. Mater. Chem.* **21**, 3655 (2011).

19. E. Schiavo, C. Latouche, V. Barone, O. Crescenzi, B. M. Garcíad, M. Pavone, *Phys. Chem. Chem. Phy.* **20**, 14082 (2018).
20. M. A. Marquardt, N. A. Ashmore, D. P. Cann, *Thin Solid Films.* **496**, 146 (2006).
21. M. Bercx, N Sarmadian, R. Saniz, B. Partoens, D. Lamoen, *Phys, Chem, Chem, Phys*. **18,** 20542 (2016).
22. A Bera, K. Deb, S. Sinthika, R. Thapa, B. Saha, *Mater. Res. Exp.* **5**, 1 (2018).
23. P. Hohenberg, W. Kohn, *Phys. Rev. B.* **136**, 864 (1964).
24. P. Giannozzi, et al., *J. Phys. Condens. Matter*. **21**, 395502 (2009).
25. J. P. Perdew, K. Burke, M. Ernzerhof, *Phys. Rev. Lett.* **77**, 3865 (1996).
26. J. D. Pack, H. J. Monkhorst, *Phys. Rev. B.* **16**, 1748 (1977).
27. R. M. Wentzcovitch, J. L. Martins, G. D. Price, *Phys. Rev. Lett*. **70**, 3947 (1993).
28. J. D. Head, M. C. Zerner, *Chem. Phys. Lett*. **122**, 264 (1985).
29. S. Baroni, S. de Gironcoli, A. D. Corso, P. Giannozzi, *Rev. Mod. Phys*. **73**, 515 (2001).
30. K. A. Mengle, S. Chae, E. Kioupakis, *J. Appl. Phys*. 126, 085703 (2019).
31. R. K. Shivade, B. Chakraborty, *Eur. Phys. J. B*. **89,** 198 (2016).
32. M. T. Dove, *Neutrons Simul.* **12**, 123 (2011).
33. P. K. Jha, S. P. Sanyal, *Physica C*. **271**, 6 (1996).
34. S. D Gupta, S. K. Gupta, P. K. Jha, N. N. Ovsyuk, *J. Raman. Spectrosc*. **44**, 926 (2013).
35. P. K. Jha, H. Soni, *J. Appl. Phys*. **115**, 023509 (2014).
36. S. D. Dabhi, S. D. Gupta, P. K. Jha, *J. Appl. Phys*. **115**, 203517 (2014).
37. T. K. Gajaria, S. D. Dabhi, P. K. Jha, *Sci. Rep*. **9,** 1 (2019).
38. E. Kroumova, M. I. Aroyo, J. M. Perez-Mato, A. Kirov, C. Capillas, S. Ivantchev, H. Wondratschek, *Phase Transit*. **76**, 155 (2003).
39. D. Upadhyay, A. Pratap, P. K. Jha, *J. Raman Spectrosc*. **50**, 603 (2019).
40. E. Cockayne, B. P. Burton, *Phys. Rev. B*. **62**, 3735 (2000).
41. R.C. Fang, *Solid Spectroscopy,* Chinese Science Technology University Press, Hefei 2003.
42. Y. Zhang, W. M. Shen, Basic of Solid Electronics, Zhe Jiang University Press, Hangzhou 2005.
43. S. Saha, T. P. Sinha, A. Mookerjee, *Phys. Rev. B.* **62**, 8828 (2000).
44. D. R. Penn, *Phys. Rev. B.* **128,** 2093 (1962).
45. A. Sajid, S. Ullah, G. Murtaza, R. Khenata, A. Manzar, S. B. Omran, J. Optoelectron, *Adv. Mater*. **16**, 76 (2014).
46. M. V. Yakushev, F. Luckert, C. Faugeras, A. V. Karotki, A. V. Mudryi, R. W. Martin, *Appl. Phys. Lett*. **97**, 152110 (2010).

47. A. S. Verma, D. Sharma, *Phys. Scr*. **76**, 22 (2007).
48. S. Bagci, B. G. Yalcin, H. A. R. Aliabad, S. Duman, B. Salmankurt, *RSC Adv*. **6,** 59527 (2016).
49. H. Salehi, E. Gordanian, *Mater. Sci. Semicond. Process*. **47**, 51 (2016).
50. N. Joshi, D. Upadhyay, A. Pandya, P. K. Jha, *J. Appl. Phys*. **126**, 235705 (2019).
51. R. Singh, R. K. Ulrich, *Electrochem. Soc. Interface.* **8**, 26 (1999).
52. Y. Wang, W. Liu, H. Chen, X. Chen, C. Liu, G. Zhuang, R. Wang, F. Shen, H. Wang, H. Xiaoyan, Z. Miao, *Phys. B.* **545**, 167 (2018).
53. M. Kumar, H. Zhao, and C. Persson, *Semicond. Sci. Technol*. **28,** 065003 (2013).
54. N. J. Szymanski, L. N. Walters, O. Hellman, D. Gall, S. V. Khare, *J. Mater. Chem. A*. **6**, 20852 (2018).
55. K. C. Bhamu, J. Sahariya, R. Vyas, K. R. Priolkar, *Pramana J. Phys*. **89,** 11 (2017).
56. K. C. Bhamu, K. R. Priolkar, *Mater. Chem. Phys.*, **190,** 114 (2017).
57. A. A. H. El-Bassuony, H. K. Abdelsalam, *J Mater Sci Mater Electron*., **29**, 5401 (2018).
58. W. Shockley, H. J. Queisser, *J. Appl. Phys*., **32**, 510 (1961).
59. M. N. Spallart, S. P. Pai, R. Pinto, *Thin Solid Films*., **515** 8641 (2007).
60. C. W. Teplin, T. Kaydanova, D. L. Young, J. D. Perkins, D. S. Ginley, A. Ode, D. W. Readey, *Appl. Phys. Lett*., **85**, 3789 (2004).
61. J. P.Porres, A. Segura, D. Kim, *Semicond. Sci. Technol*., **24,** 015002 (2009).
62. B. G. Kim, E. Garmire, S. G.Hummel, P. D. Dapkus, *Appl. Phys. Lett*., **54,** 12 (1989).
63. A. S. Prakash, D. Larcher, M. Morcrette, M. S. Hegde, J. B. Leriche, C. Masquelier, *Chem. Mater*., **17**, 4406 (2005).
64. G. A. Costa, E. Kaiser, *Thermochim. Acta*., **269,** 591 (1995).